as one of the important causes of implant failures.[10,11] However, a causative relationship between implant failure and occlusal forces has not been convincingly demonstrated.[12,13] Animal studies provided conflicting results in this issue. Under extensive occlusal and cyclic loading, marginal bone resorption has been demonstrated in the absence of peri-implant tissue inflammation.[10,14,15] However, experimental studies using different animal models have shown that occlusal stress does not cause significant peri-implant bone loss in the absence of peri-implant infection.[16,17]

Although various attempts have been made to assess the effect of occlusal loads on peri-implant bone loss, the "overloading" has not been well defined in terms of mechanical stress at the bone–implant interface. Because the progress of the marginal bone loss occurs as a result of the bone resorption or loss of the bone–implant contact at the interface (interfacial failure), the magnitude and direction of the stress should be fully investigated to assess potential association between the overloading and the marginal bone loss.

The objective of this study is to assess the effects of microthread design and loading angle on the direction and magnitude of the interfacial, principal (stresses in the principal planes), and shear stresses at the bone–implant interface around the implant. The results were analyzed to understand stress-transferring mechanisms from different implant surfaces to the supporting bone, and to test a hypothesis that the microthread structure reduces the risk of interfacial failures.

MATERIALS AND METHODS

Construction of Three-Dimensional Models

Three-dimensional FE models representing two implants, one with microthreads in the neck region and the other with a smooth neck, were constructed. A microthreaded implant§ with 4-mm diameter and 11-mm length was scanned under a microscope‖ and imported into image analysis software.¶ The outline of the implant was plotted and converted into x and y coordinates, which were imported into the FE software# as keypoints (Fig. 1). For the smooth-neck implant, which served as control, the outline was created by connecting the tops of the microthreads of the microthread model. The two-dimensional images were then extruded around their central axis to produce axisymmetric three-dimensional FE models. The implants were connected to abutment** and simplified cylindrical crown of 7.5-mm height and 5.5-mm diameter, which were created using the same procedure as for the implant.

A three-dimensional FE model of a mandibular bone segment was created based on the most common morphologic model among the nine classification groups for the mandibular premolar region in our previous study.[18]

Average dimensions of the cross-sectional outlines at the premolar region based on computed tomography images of 36 patients of that morphology group were used to create x and y plots that described the outline of the external cortical bone surface. The area made from the outline was divided into a cancellous core surrounded by a uniform 1.5-mm thick cortical bone. Each image on the x–y plane was extruded to the z axis to create a three-dimensional model with 15-mm mesio-distal length. Because of the mesio-distal symmetry, only the distal half of the model was constructed.[19,20]

The vertical dimension and the maximum bucco-lingual width of the mandible model at the first premolar region where the implant is being installed were 28.6 and 13.9 mm, respectively. Each implant was vertically embedded on top of the alveolar ridge. The central axis of each implant positioned at the bucco-lingual center. The vertical position was determined so that the microthread was embedded at the highest level of the alveolar crest in the distal cervical bone; this resulted in exposure of a thread at the buccal and lingual ridges.[21]

Material Properties, Meshing, Boundary, and Loading Conditions

The material properties of cortical and cancellous bone were modeled as being transversely isotropic and linearly elastic,[22,23] which describes an anisotropic material. The materials of the implant and prosthetic crown were assumed to be isotropic and linearly elastic with Young moduli and Poisson ratio of 107 GPa and 0.3 for the implant and of 96 GPa and 0.35 for the prosthetic crown, respectively.

A 20-node tetrahedral element was used for the mesh. To determine the valid element numbers and mesh sizes, the convergence test for consistency of solutions was conducted for each model.[24] Two variables were tested: the maximum third principal stress and the volume of cortical bone that exhibited compressive strain >4,000 μ. The mesh was refined several times by reducing the edge size for elements to increase the numbers of nodes at the bone–implant interface where the maximum stress and strain appeared. The least number of elements, over which the variable measures became plateau, was used in this study.

The symmetric boundary conditions were prescribed at the nodes on the mesial plane of the distal half of each model. The models were constrained in all

§ AstraTech Microthread 4.0 ST, Astra Tech AB, Mölndal, Sweden.
‖ BZ-8000, Keyence Corporation, Osaka, Japan.
¶ Image J, National Institutes of Health, Bethesda, MD.
# ANSYS11.0, ANSYS, Canonsburg, PA.
** TiDesign 3.0, Astra Tech AB.

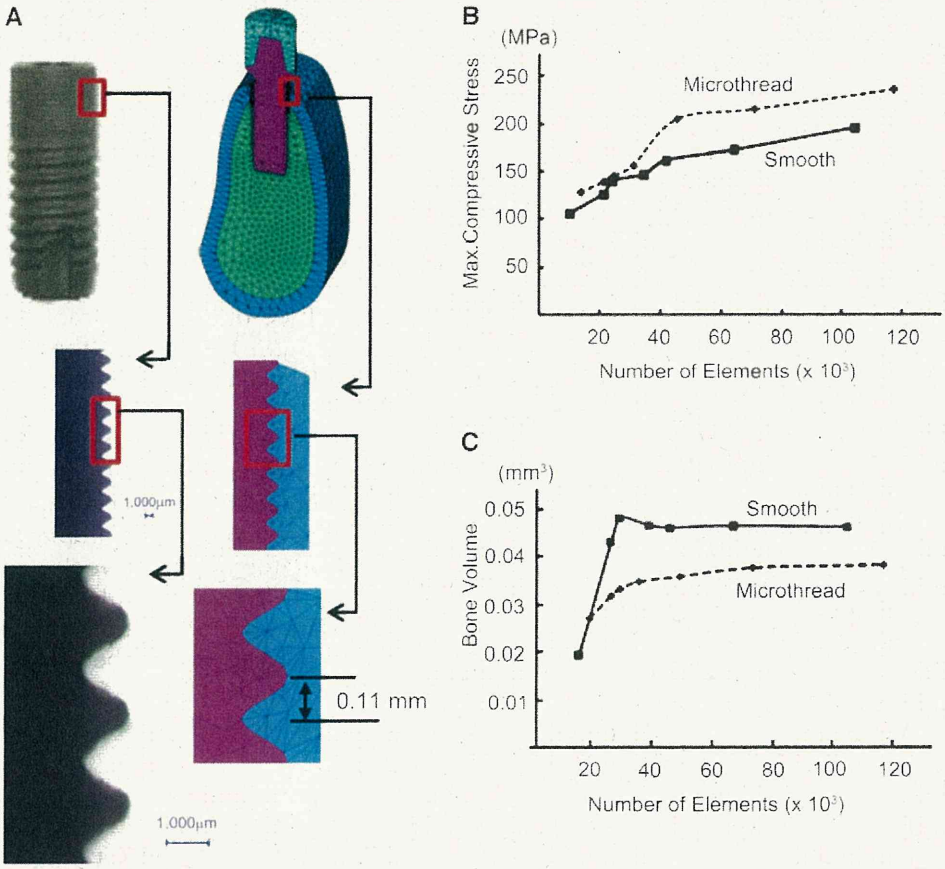

Figure 1.
*The meshed FE model of the implant and the bone **(A)** and the convergence tests **(B** and **C)**. Cancellous bone (green mesh) surrounded by a layer of cortical bone (blue mesh). Light microscopic images of the microthread morphology in the implant fixture were traced to create the neck part of the three-dimensional FE model of the implant (A). The convergence test of the microthread and smooth implant neck models of this study. The maximum third principal stress at the crestal bone (B) and bone volumes that exhibited the maximum compressive strain >4,000 μ (C) were used as the variable measures. Seven iterations by mesh refinement were calculated up to 120,000 elements for each model.*

directions at the nodes on the distal bone surface. The implants were rigidly anchored in the bone models along the entire interface, and the same type of contact was provided at the prosthesis–abutment interface. A static load in one of the four directions (vertical [0°], 30°, and 60° oblique from buccal to lingual, and horizontal [90°] angles to the long axis of each implant) was applied to the center of the occlusal surface of the superstructure. However, the 30° oblique load, which corresponded with the direction of occlusal forces in the premolar region was used for general discussion. Because the point of load application is included in the symmetry boundary conditions, each input load was doubled during computations. The resultant load (200 N) was used to simulate the average maximum occlusal load for fixed partial prosthesis supported by implants in the premolar region.[25] The directions and magnitudes of the maximum compressive (third or minimum principal stress), tensile (first or maximum principal stress), and shear stress and strain generated in the bone were analyzed.

RESULTS

For the convergence tests, seven iterations by mesh refinement were calculated for each model. The peak compressive stress values and the bone volume that exhibited a high compressive strain >4,000 μ as a function of the number of elements are shown in Figures 1B and 1C. As the number of elements increased, both models revealed an increase in the peak compressive stress without showing a plateau even with using ≈120,000 elements. The curves of the high strain bone volumes revealed a well-developed plateau after the number of elements was >≈40,000. This indicates that the volume of high strain is insensitive to further refinement of the mesh. Based on these results, the element edge size was set equal to 0.03 mm for the interface. Accordingly, the final microthread model was composed of 70,060 elements and 13,867 nodes, and the smooth model was of 63,568 elements and 13,744 nodes.

The compressive, shear, and tensile stress distributions in the bone under the 30° oblique load are shown in Figure 2. The location of the maximum stress in the smooth model was at the top of the crestal cortical bone attached to the mesio-distal center of the implant, whereas those of the peak compressive and shear stresses in the microthread model were deviated distally from the mesio-distal center (black arrows in the Fig. 2).

Figure 3 shows the peak compressive stress appeared in the region right under the flank of the first microthread, which was exposed from the crestal edge in the disto-lingual region. The maximum stress values in the microthread and smooth models on the lingual and buccal crestal bone under all loading angles are shown in Table 1.

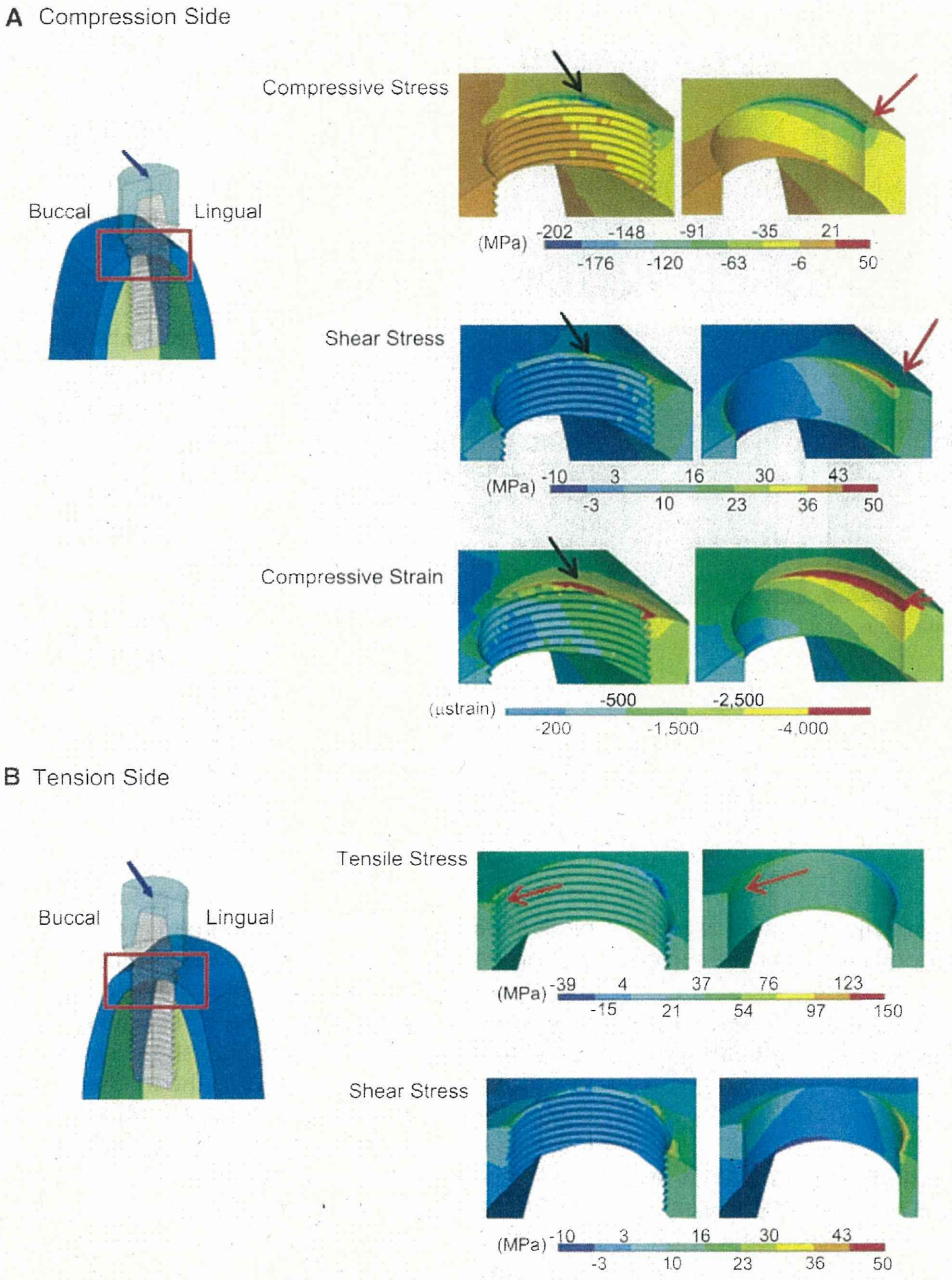

Figure 2.
A *and* ***B)*** *The compressive, tensile, and shear stress distributions and the compressive strain distributions in the cervical cortical bone under the 30° oblique load with microthread and smooth models. The distal half of each symmetric section is viewed from the mesial side, with the focus on the interfacial bone surface. Figures on the left indicate the viewing angle and the region (red square) in the contour graphics on the right. Blue arrows indicate the direction of occlusal forces. Each contour graphic was divided into nine parts, with different colors according to the stress or strain levels, shown in a scale below each figure. Red arrows indicate the location of the maximum stress that appeared at the mesio-distal center of each implant. Black arrows indicate the location of the maximum stress that deviated from the mesio-distal center of each implant.*

The principal stresses at each node in the cortical bone were shown in the form of stress arrows on the bucco-lingual section at the mesio-distal center of each implant (Fig. 4). Under the vertical loading, the compressive stress was evenly distributed on both sides of the interface, with the highest stress located at the top of the ridge. In the microthread model, large compressive stresses were shown mostly under the lower flank of each microthread and the directions of the stresses were perpendicular to the thread surface, whereas in the smooth model the directions of the interfacial compressive stresses were oblique (with 58.4°) to the interface. Under the oblique or horizontal loadings, the compressive and tensile stresses were dominantly distributed on the lingual and buccal sides, respectively. The stresses were again perpendicular to the lower surface of each microthread, whereas in the smooth model the stress directions were oblique to the interface with 50.5°, 45.1°, and 46.8° under the 30°, 60°, and horizontal loading, respectively.

The peak compressive and shear stresses on the interface along the lingual wall and the peak tensile and shear stresses along the buccal wall, both at the mesio-distal center under the 30° oblique load, are graphed in Figure 5. All stresses peak at the top of the crestal bone. The microthread model exhibited decreases of the stresses with a wavy pattern as downward along the interface, whereas the stresses in the smooth model decreased with a gradual curve. In the wavy curve of the microthread model, the bottom of each wave corresponded to the thread root, whereas the prominence of each wave corresponded to the point where the lower flank passes to the curved thread crest. The microthread model indicated lower peak stresses than the smooth model along the whole interface, except for the tensile

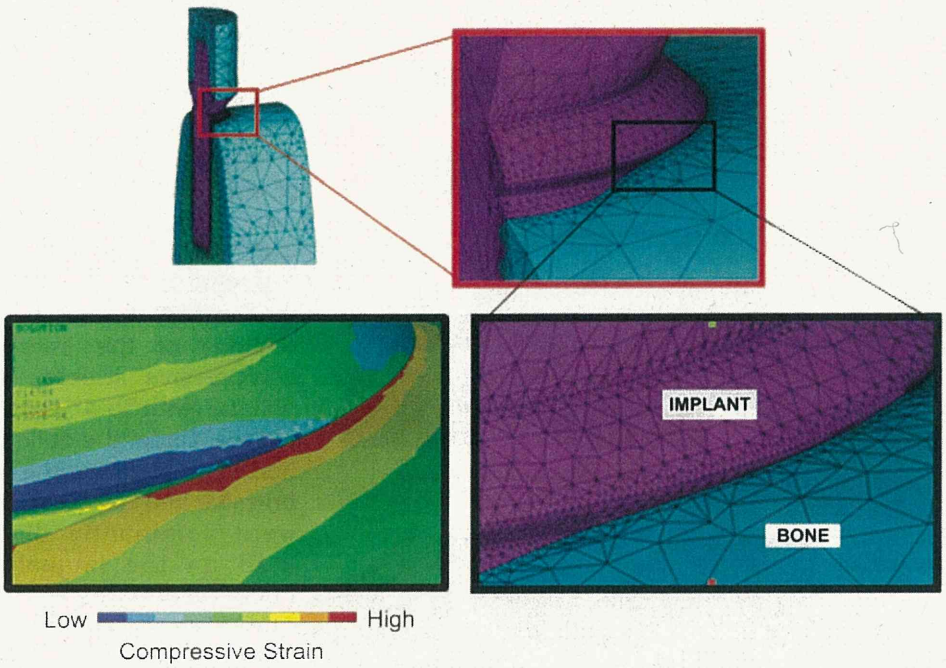

Figure 3.
The maximum compressive strain distributions of the microthread and the crestal bone in the disto-lingual surrounding of the microthread implant. The maximum compressive strain of the bone appeared in the region just under the first microthread that was exposed from the crestal edge.

stress in the lower flank of the microthreads, which was higher than that in the smooth model at the same vertical level.

The peak compressive strains of the bone along the interface on the lingual and buccal sides are shown in Table 1.

DISCUSSION

Altering the surface structure of dental implants is an effective way to preserve the peri-implant marginal bone.[26] Microthread design is considered as a retentive element and macro-roughness[1] has demonstrated the beneficial effect of reducing marginal bone resorption in clinical and animal studies.[3,6]

The effect of loading angle on the magnitude and directions of the interfacial stress around the microthread implant was not clear. Although the implant fixtures are usually installed perpendicularly to the occlusal plane, implants are susceptible also to oblique and horizontal loading. These loads on the implant create two typically shown stress fields in the crestal bone: the compression and tension fields, which are located on the opposite sides across the implant and characterized by domination of the principal compressive and tensile stresses, respectively. Such stress fields are also created in the periodontal structures of a natural tooth,[27] but are different from those of the implant vicinity, in that the periodontal ligament acts as a cushion and absorbs tensile and compressive stresses. In contrast, the bone–implant interface is so rigid that the stress increases on the off-axis loading and potentially causes interfacial failures.[28] To comprehensively evaluate the biomechanical aspects of microthread design, the magnitude and direction of different interfacial stresses along with high-strain bone volumes under different loading angles were analyzed in this study.

On vertical loading, the microthread implant showed lower compressive but higher shear and tensile stress values compared to the smooth implant. These results disagree with a previous FE study[1] in which vertical forces only were applied and resulted in lower peak shear stress in the microthread model. This disagreement is probably because of the differences in the morphology of the alveolar bone and material properties assigned. However, a marked increase in the first and third principal and shear stress values in both models was observed as the loading angle increased in the oblique and horizontal loading cases. Off-axis loading was found to be more destructive to the bone–implant interface.[29-31] Interestingly, under off-axis loading, the microthread implant in this study generated lower maximum shear but higher compressive stress values.

Also, the direction of the principal stresses at the microthread interface was consistently perpendicular to the lower thread flank regardless of the loading direction. In contrast, the direction of the principal stresses in the smooth model was oblique to the interface and affected by the loading angle. As the loading angle increased (i.e., larger horizontal component), interfacial stresses tended to be more oblique to the interface.

Oblique interfacial stress direction represents a resultant force that can be analyzed into the two basic force components: the first is perpendicular to the interface and represents the compressive or tensile stress, and the second is parallel with the interface and represents the shear stress. According to this

Table 1.

Maximum Stress and Strain Values in the Compressive and Tensile Halves of the Crestal Bone Surrounding the Microthread and Smooth Implant Under Vertical, 30°, 60° Oblique, and Horizontal Loading

		Compressive Side					Tensile Side	
Model	Force Direction (degree)	Compressive Stress (MPa)	Tensile Stress (MPa)	Shear Stress (MPa)	Compressive Strain (μ strain)	Large Strain Volume (mm^3)	Tensile Stress (MPa)	Shear Stress (MPa)
Microthread	0	42.49	87.77	28.95	4,740	1.38E-04	77.41	1.6
	30	201.9*	142.1	44.6*	10,990*	0.033431	70.1	21.8
	60	259.6	116.5	63.7	14,515	0.215624	183.3	52.2
	90	248.0	137.3	65.7	14,176	0.219261	248.1	68.94
Smooth	0	87.6	59.6	21.3	3,898	0	59.1	2.7
	30	140.8	81.7	49	8,214	0.041591	58.7	25.3
	60	201.6	95.4	83.5	14,041	0.244157	145.1	59.2
	90	206.3	80.4	85.7	14,373	0.242616	199.8	78.2

The maximum values were indicated at the mesio-distal center of the implants, except for the maximum compressive and shear stresses and the maximum compressive strain in the microthread model (asterisks). The large strain volume represents the region of the cortical bone that showed the maximum compressive strain >4,000 μ.

analysis, considerable amount of shear stress is transmitted across the smooth interface, whereas for the microthread implant loads are transferred to compressive stresses (at the compression side) perpendicular to the lower flank of each microthread. These results were confirmed by the stress profiles along the bone–implant interface (Fig. 5).

Transferring occlusal loads into compressive stress around the microthread implant can provide a significant benefit because bone is most resistant against the compressive forces.[32] Interfacial failure and bone resorption under different stress types is attributed to different mechanisms. Accordingly, it may be erroneous to emphasize the peak compressive or von Mises equivalent stresses without considering the risks of the tensile and the shear stresses at the interface.

The results of this analysis revealed that incorporating microthreads in the implant neck resulted in higher peak compressive stress and strain values in the peri-implant bone structures under off-axis loading. These findings are consistent with those of a previous two-dimensional FE study in which maximum von Mises stress was higher in the crestal bone around microthread implant.[8] However, the high stress and strain magnitude were found to be limited to a small region localized at the crestal bone around the implant neck. Although the estimation of the maximum equivalent (von Mises) and the principal stresses has been frequently used to assess failure risks of biomaterials and the peri-implant bone tissues, evaluating the bone volume that exhibited high stress or strain and the stress distribution pattern along the interface may reflect more realistic quantitative and qualitative measures for bone resorption risks. Moreover, the results of the convergence tests suggest that the peak stress that is usually used in previous comparisons was highly dependent of the mesh size, and thus does not ensure validity for quantitative evaluation of the biomechanical risks.

The compressive strain has often been used as a risk scale on the basis that bone resorption under compressive forces is attributed to the accumulation of induced microdamage that exceeds the bone's capacity of repair. The volume of the high strain level >4,000 μ, which is regarded as a mechanical stimulation that potentially causes pathologic overloading to the bone,[33] was very small for both microthread and smooth models, but relatively larger in the case of the smooth-neck model. This may cancel the proposed advantage of the lower stress and strain values around the smooth-neck implant, which was reported in the previous study[8] and confirmed in this research.

Incomplete coverage of implant microthreads or macrothreads may result because of the narrow dimension of the crestal region and the curved nature of the alveolar bone. This is considered to be an acceptable situation as reported in previous clinical studies with different follow-up periods.[21,34] The three-dimensional modeling of the implant and the bone in this study allowed for simulating this situation, which was not shown in the previous two-dimensional models. In the microthreaded implant, the peak compressive stress was shifted from the mid line to the exposed thread region. The location of peak stress in

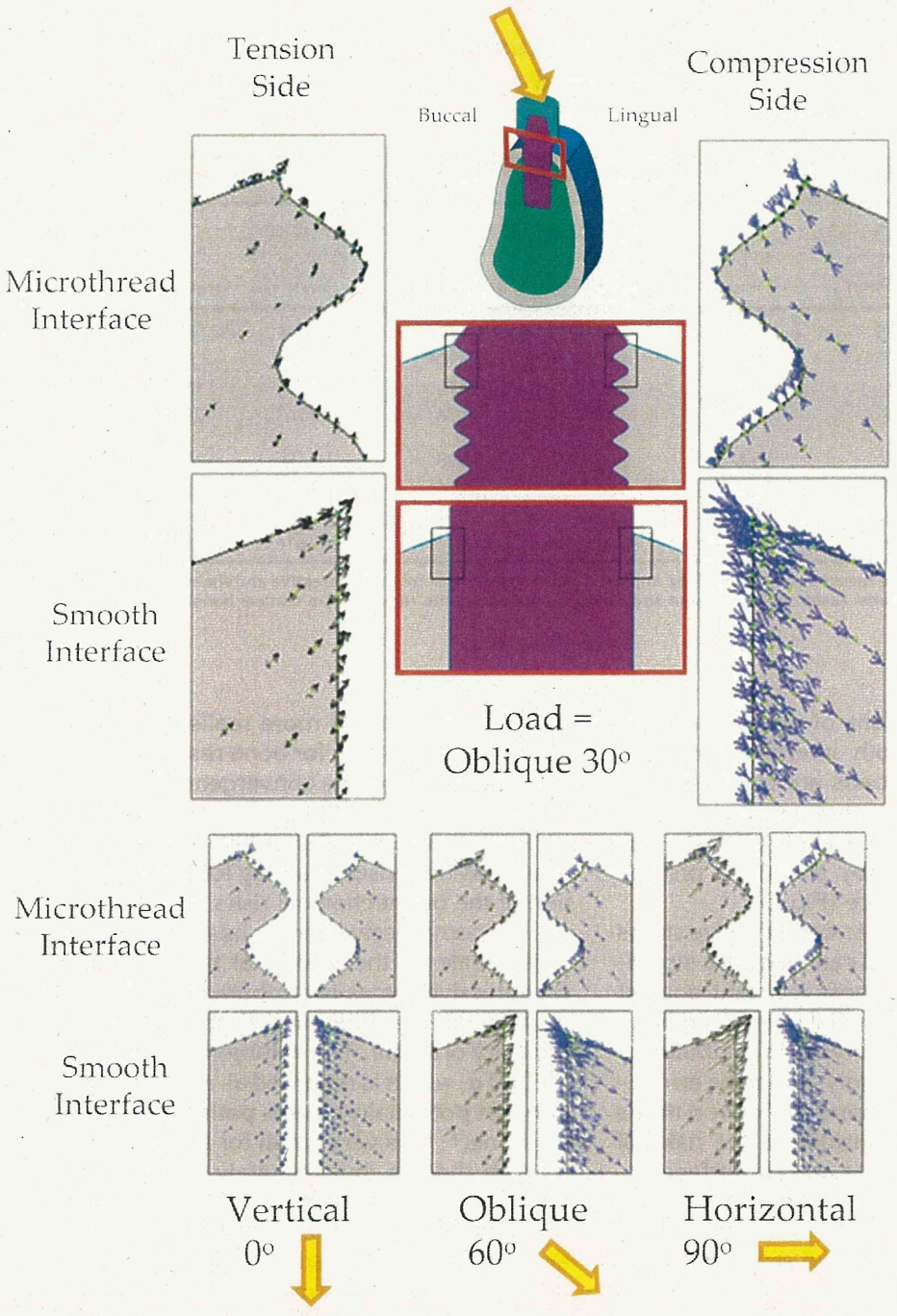

Figure 4.
Stress arrow graphics at the cervical level of the cortical bone on the tension and compression sides. The direction and magnitude of the principal stress at each element in the crestal bone of the buccal (tension) and lingual (compression) sides are shown in the bucco-lingual section at the mesio-distal center of each implant under vertical (0°), 30° oblique, 60° oblique, and horizontal (90°) loadings. Black arrows represent the first principal (tensile) stress; blue arrows indicate the third principal (compressive) stress. Length of each arrow represents relative magnitude of stress that is projected on the two-dimensional plane. Figures with black and red squares in the middle indicate the site of the arrow graphics.

this study consists of that shown in a previous FE study.[35] It is now clear that the location of the first thread relative to the bone surface affects the stress distribution in the cervical region; however, the effect was limited to this region and did not seem to have a negative effect because the volume of bone that exhibited high strain (red area in Fig. 2) was smaller in the microthread model than in the smooth model (Table 1).

However, in this study, the modeling of the bone–implant interface was performed on the assumption of a perfect bonding because no detachment was allowed under tensile or shear stresses. This has been assumed because of the absence of reliable interfacial tensile and shear strength data. Regarding the bone–implant interfacial tensile strength, previous studies reported a range of 1 to 4 MPa;[28] however, in most of these studies, a flat implant model was used and the variability in bone–implant contact percentage was not considered. Bone–implant contact percentage greatly varies among different surfaces and designs. However, the debonding at the tension side has never been reported clinically under functional occlusal forces. Moreover, because the microthreaded implants have shown larger bone–implant contact percentage,[3] it is expected that microthreaded implants will have larger interfacial tensile strength.

Furthermore, comparing the results of this study with the available bone–implant interfacial shear strength to predict whether there will be debonding or sliding of the

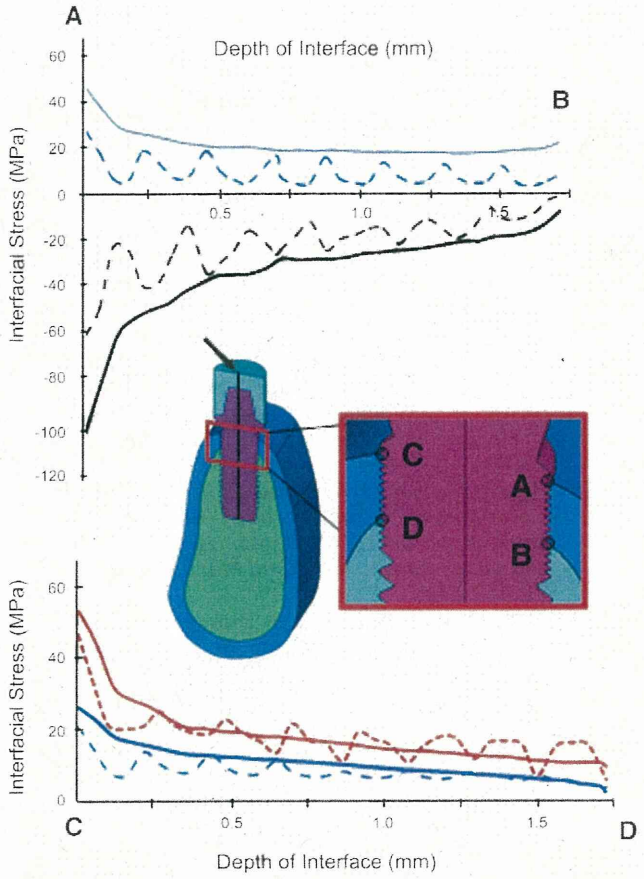

Figure 5.
Interfacial stresses on the compression (upper graphs) and tension (lower graphs) sides under the 30° oblique load. The bone–implant interfacial compressive (black), shear (blue), and tensile (red) stresses in the cortical bone along the lingual wall for compressive side of the microthreaded model (dashed lines) and smooth model (solid lines) under the 30° oblique load. The shear and tensile stresses were represented as positive values, whereas the compressive stress was shown as negative values.

implant (i.e., failure of the interface because of shear stress) may not be applicable. This is actually because of the simplicity of methods used in this issue. For example, most push-out tests did not really measure the shear strength of the bone–implant interface; instead, they reported a value that although called "pushout strength," is a combination of various fixation principles (friction, mechanical interlock, and chemical bonding).[36,37] Accordingly, the debonding was not allowed in this study under shear stress.

In addition, cyclic fatigue loading should be considered if a structural model was made to account for changes in the bone–implant interface with degradation or failure of osseointegration. An earlier animal study described a greater bone response revealed when rabbit tibiae was loaded dynamically than statically.[14]

Further biologic studies regarding the effects of the tensile and shear stresses on the interfacial failure are encouraged to establish a comprehensive understanding of the role of occlusal loads in preserving peri-implant tissues.

The findings of this study demonstrated the effectiveness of the microthread design not only in withstanding off-axis loading but also supporting the hypothesis of the effect of threads in transforming shear stress into a compressive stress. Reducing shear stress under off-axis loading indicates the benefit of microthread design especially when a larger horizontal force component is expected, such as in the anterior maxillary region[38] or when implants are tilted because of the presence of anatomic limitations.[39]

CONCLUSIONS

Off-axis occlusal loads create compression and tension fields in the crestal bone, and are typically located on the opposite sides across the implant. In the smooth-surface implant, the direction of the principal stresses at the bone–implant interface was found to be oblique to the interface and affected by the loading angle, whereas those were consistently perpendicular to the lower flank of microthreads under different loading angles in the microthread implant, suggesting that the stress at the microthread interface was insensitive to the loading angle and indicating larger shear stress at the bone–implant interface around the smooth implant. Also, the microthread design was found to be more effective in reducing shear stress under off-axis loading, which dominates in the oral cavity. However, higher peak compressive stress and strain around the microthread implant were found to be localized in a smaller bone volume compared to the smooth implant. These results collectively might demonstrate the biomechanical rationale of microthread design over smooth surfaces in reducing the risks of marginal bone loss caused by overloading.

ACKNOWLEDGMENTS

This study was supported by the Grants-in-Aid for Scientific Research #20592307 (NW) and High-Tech Research Project 2005 to 2009 grants from the Japan Society for the Promotion of Science/The Ministry of Education, Culture, Sports, Science and Technology of Japan. The authors report no conflicts of interest related to this study.

REFERENCES

1. Hansson S. The implant neck: Smooth or provided with retention elements. A biomechanical approach. *Clin Oral Implants Res* 1999;10:394-405.

2. Rasmusson L, Kahnberg KE, Tan A. Effects of implant design and surface on bone regeneration and implant stability: An experimental study in the dog mandible. *Clin Implant Dent Relat Res* 2001;3:2-8.
3. Abrahamsson I, Berglundh T. Tissue characteristics at microthreaded implants: An experimental study in dogs. *Clin Implant Dent Relat Res* 2006;8:107-113.
4. Berglundh T, Abrahamsson I, Lindhe J. Bone reactions to longstanding functional load at implants: An experimental study in dogs. *J Clin Periodontol* 2005; 32:925-932.
5. Wennström JL, Ekestubbe A, Gröndahl K, Karlsson S, Lindhe J. Implant-supported single-tooth restorations: A 5-year prospective study. *J Clin Periodontol* 2005; 32:567-574.
6. Lee DW, Choi YS, Park KH, Kim C-S, Moon I-S. Effect of microthread on the maintenance of marginal bone level: A 3-year prospective study. *Clin Oral Implants Res* 2007;18:465-470.
7. Palmer RM, Palmer PJ, Smith BJ. A 5-year prospective study of Astra single tooth implants. *Clin Oral Implants Res* 2000;11:179-182.
8. Schrotenboer J, Tsao YP, Kinariwala V, Wang HL. Effect of microthreads and platform switching on crestal bone stress levels: A finite element analysis. *J Periodontol* 2008;79:2166-2172.
9. Hansson S, Halldin A. Re: effect of microthreads and platform switching on crestal bone stress levels: A finite element analysis (letter to the editor). *J Periodontol* 2009;80:1033-1035; authors' response 1035-1036.
10. Isidor F. Loss of osseointegration caused by occlusal load of oral implants. A clinical and radiographic study in monkeys. *Clin Oral Implants Res* 1996;7: 143-152.
11. Isidor F. Histological evaluation of peri-implant bone at implants subjected to occlusal overload or plaque accumulation. *Clin Oral Implants Res* 1997;8:1-9.
12. Carlsson GE. Critical review of some dogmas in prosthodontics. *J Prosthodont Res* 2009;53:3-10.
13. Hobkirk JA, Wiskott HWA, Working Group 1. Biomechanical aspects of oral implants. Consensus report of Working Group 1. *Clin Oral Implants Res* 2006; 17(Suppl. 2):52-54.
14. Duyck J, Rønold HJ, Van Oosterwyck H, Naert I, Vander Sloten J, Ellingsen JE. The influence of static and dynamic loading on marginal bone reactions around osseointegrated implants: An animal experimental study. *Clin Oral Implants Res* 2001;12:207-218.
15. Miyata T, Kobayashi Y, Araki H, Ohto T, Shin K. The influence of controlled occlusal overload on peri-implant tissue. Part 3: A histologic study in monkeys. *Int J Oral Maxillofac Implants* 2000;15:425-431.
16. Gotfredsen K, Berglundh T, Lindhe J. Bone reactions adjacent to titanium implants subjected to static load. A study in the dog (I). *Clin Oral Implants Res* 2001;12: 1-8.
17. Miyata T, Kobayashi Y, Araki H, Motomura Y, Shin K. The influence of controlled occlusal overload on peri-implant tissue: A histologic study in monkeys. *Int J Oral Maxillofac Implants* 1998;13:677-683.
18. Hudieb MI, Wakabayashi N, Suzuki T, Kasugai S. Morphologic classification and stress analysis of the mandibular bone in the premolar region for implant placement. *Int J Oral Maxillofac Implants* 2010;25: 482-490.
19. Petrie CS, Williams JL. Comparative evaluation of implant designs: Influence of diameter, length, and taper on strains in the alveolar crest. A three-dimensional finite-element analysis. *Clin Oral Implants Res* 2005;16:486-494.
20. Kitamura E, Stegaroiu R, Nomura S, Miyakawa O. Influence of marginal bone resorption on stress around an implant — A three-dimensional finite element analysis. *J Oral Rehabil* 2005;32:279-286.
21. Veltri M, Ferrari M, Balleri P. One-year outcome of narrow diameter blasted implants for rehabilitation of maxillas with knife-edge resorption. *Clin Oral Implants Res* 2008;19:1069-1073.
22. O'Mahony AM, Williams JL, Spencer P. Anisotropic elasticity of cortical and cancellous bone in the posterior mandible increases peri-implant stress and strain under oblique loading. *Clin Oral Implants Res* 2001;12:648-657.
23. Huang HL, Chang CH, Hsu JT, Fallgatter AM, Ko CC. Comparison of implant body designs and threaded designs of dental implants: A 3-dimensional finite element analysis. *Int J Oral Maxillofac Implants* 2007; 22:551-562.
24. Al-Sukhun J, Kelleway J. Biomechanics of the mandible: Part II. Development of a 3-dimensional finite element model to study mandibular functional deformation in subjects treated with dental implants. *Int J Oral Maxillofac Implants* 2007;22:455-466.
25. Mericske-Stern R, Assal P, Mericske E, Bürgin W. Occlusal force and oral tactile sensibility measured in partially edentulous patients with ITI implants. *Int J Oral Maxillofac Implants* 1995;10:345-353.
26. Norton MR. Marginal bone levels at single tooth implants with a conical fixture design. The influence of surface macro- and microstructure. *Clin Oral Implants Res* 1998;9:91-99.
27. Ona M, Wakabayashi N. Influence of alveolar support on stress in periodontal structures. *J Dent Res* 2006; 85:1087-1091.
28. Brunski JB. In vivo bone response to biomechanical loading at the bone/dental-implant interface. *Adv Dent Res* 1999;13:99-119.
29. Hsu ML, Chen FC, Kao HC, Cheng CK. Influence of off-axis loading of an anterior maxillary implant: A 3-dimensional finite element analysis. *Int J Oral Maxillofac Implants* 2007;22:301-309.
30. Kim Y, Oh TJ, Misch CE, Wang HL. Occlusal considerations in implant therapy: Clinical guidelines with biomechanical rationale. *Clin Oral Implants Res* 2005; 16:26-35.
31. Sütpideler M, Eckert SE, Zobitz M, An KN. Finite element analysis of effect of prosthesis height, angle of force application, and implant offset on supporting bone. *Int J Oral Maxillofac Implants* 2004;19:819-825.
32. Guo EX. Mechanical properties of cortical bone and cancellous bone tissue. In: Cowin SC, ed. *Bone Mechanics Handbook*. Boca Raton, FL: CRS press; 2001:10/1-23.
33. Frost HM. From Wolff's law to the mechanostat: A new "face" of physiology. *J Orthop Sci* 1998;3:282-286.
34. Lekholm U, Sennerby L, Roos J, Becker W. Soft tissue and marginal bone conditions at osseointegrated implants that have exposed threads: A 5-year retrospective study. *Int J Oral Maxillofac Implants* 1996;11: 599-604.

35. Hansson S, Werke M. The implant thread as a retention element in cortical bone: The effect of thread size and thread profile. A finite element study. *J Biomech* 2003; 36:1247-1258.
36. Black J. "Push-out" tests. *J Biomed Mater Res* 1989; 23:1243-1245.
37. Dhert WJ, Verheyen CC, Braak LH, et al. A finite element analysis of the push-out test: Influence of test conditions. *J Biomed Mater Res* 1992;26:119-130.
38. Weinberg LA. Therapeutic biomechanics concepts and clinical procedures to reduce implant loading. Part I. *J Oral Implantol* 2001;27:293-301.
39. Woo I, Le BT. Maxillary sinus floor elevation: Review of anatomy and two techniques. *Implant Dent* 2004;13: 28-32.

Correspondence: Dr. Malik Hudieb, Department of Oral Implantology and Regenerative Dental Medicine, Tokyo Medical and Dental University, 1-5-45 Yushima, Bunkyo, Tokyo 113-8549, Japan. Fax: 81-3-58034664; e-mail: malik.i.h.irm@tmd.ac.jp.

Submitted April 23, 2010; accepted for publication November 29, 2010.

Int. J. Oral Maxillofac. Surg. 2011; 40: 200–206
doi:10.1016/j.ijom.2010.10.002, available online at http://www.sciencedirect.com

International Journal of
Oral & Maxillofacial Surgery

Research Paper
Imaging Technology

Biomechanical effect of crestal bone osteoplasty before implant placement: a three-dimensional finite element analysis

M. Hudieb[1,2], S. Kasugai[1,2]
[1]Department of Oral Implantology and Regenerative Dental Medicine, Division of Oral Health Sciences, Graduate School, Tokyo Medical and Dental University, Japan; [2]Global Center of Excellence Program, International Research Center for Molecular Science in Tooth and Bone Diseases, Tokyo Medical and Dental University, Japan

M. Hudieb, S. Kasugai: Biomechanical effect of crestal bone osteoplasty before implant placement: a three-dimensional finite element analysis. Int. J. Oral Maxillofac. Surg. 2011; 40: 200–206.

Abstract. This study investigated the biomechanical effects of crestal bone osteoplasty and flattening procedures carried out in edentulous knife-edge ridges to restore bone width before implant placement on the virtually placed implants using finite element methods. Three-dimensional models representing a knife-edged alveolar bone with two different crestal cortical bone thicknesses (1.6 mm, thin group; 3.2 mm, thick group) were created. Gradual crestal bone osteoplasty with 0.5 mm height intervals was simulated. Cylindrical implants with abutments and crowns were constructed and subjected to oblique loads. Maximum stress was observed at the cervical region around the implant neck. Different osteoplasty levels showed different stress values and distributions. Highest compressive stress was observed in the flat models (60.8 MPa and 98.3 MPa in thick and thin groups, respectively), lowest values were observed when osteoplasty was limited to the sharp edge (36.8 MPa and 38.9 MPa in thick and thin groups, respectively). The results suggested that eliminating the sharp configuration in knife-edge ridges improved stress and strain outcomes, but flattening the alveolar crest and/or uncovering the cancellous bone resulted in a marked increase in compressive stress and strain values in the peri-implant bone that may influence the longevity of implants placed in these ridges.

Keywords: osteoplasty; dental implant; knife edge ridge; bone stress; strain; finite element analysis.

Accepted for publication 5 October 2010
Available online 4 December 2010

Dental implants have been widely used for prosthetic rehabilitation of partially and completely edentulous patients. Adequate available bone dimensions are considered a prerequisite for successful and predictable implant treatment[1,3]. Following tooth extraction, continuous bone resorption usually takes place and results, initially, in a narrow ridge with a knife-edge form[4,7].

A relatively large percentage of narrow ridges with knife-edge configuration have been reported at the edentulous mandibular and maxillary bony crests[2,1]. Treatment for completely removable dentures may require preprosthetic surgical reduction of the sharp edges to prevent painful denture pressure points at the knife-edged borders. Increasing the horizontal width of the bone prior to implant placement is required in these ridges to host the implant in the alveolar bone properly[16,21]. This can be achieved by osteoplasty, performed to eliminate and flatten the thin sharp edge configuration, and/or additional bone augmentation and surgical procedures such as onlay bone grafts[5], guided bone regeneration[3] horizontal distraction[25] and

0901-5027/020200+07 S36.00/0

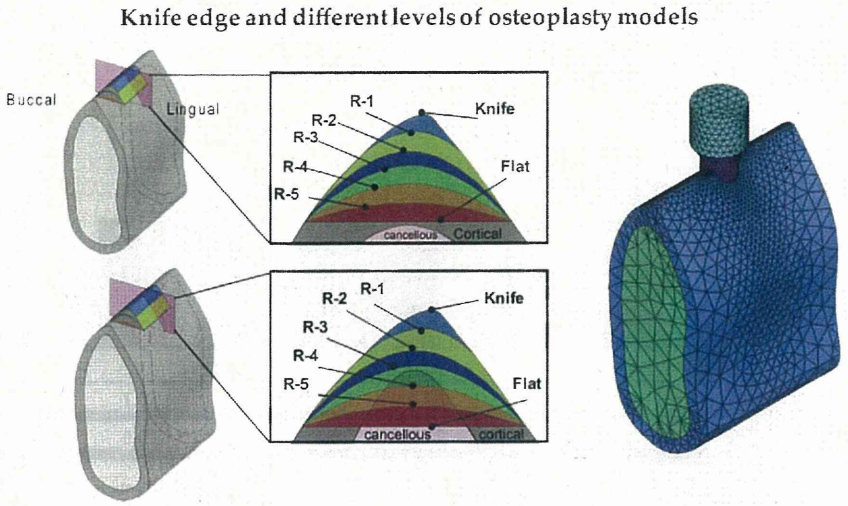

Fig. 1. Basic mandibular bone segments used for the thin and thick cortical bone groups. Simulation of flattening and several levels of osteoplasty in the middle part of the bone segment are shown in the cross-sectional image. The name of each model refers to the outer bone curvature used. Cancellous bone was exposed in R4, R5 and Flat models of the thin cortical bone group. The meshed FE model of the thick knife edge bone is shown on the right.

sagittal osteotomies of the edentulous ridge[5].

When the narrow width is limited to the alveolar bone crest in ridges with adequate height, osteoplasty or flattening procedures are recommended rather than bone augmentation procedures[16]. The local anatomy and geometry of the peri-implant bone influence the distribution and intensity of the stresses generated in the surrounding bone, because of the mechanical interlocking relationship between the implant and the surrounding bone[10,19]. Excessive stresses generated around dental implants are considered to be one of the main causes of peri-implant bone loss and/or implant failure[6,12].

The effect of crestal bone osteoplasty and the flattening procedures that precede implant placement on the biomechanical behavior of dental implants has not been assessed in relation to the stress and strain generated around the dental implants that will be placed in these ridges. The purpose of this study was to evaluate the biomechanical effect of surgical reduction and flattening of the narrow alveolar bone crest on the biomechanical behavior of the future implants using three dimensional (3D) finite element analysis (FEA). Several methods have been used to evaluate the biomechanical aspect of dental implants such as FEA, strain gauges and photo-elastic models. Of these methods, FEA is considered the method of choice to calculate the stresses generated in complex geometries and to evaluate different variables simultaneously[9].

Materials and methods

Model design

A 3D model of an edentulous mandibular segment with knife-edge configuration was constructed. A cross-sectional CT scan for the mandibular first premolar region was selected with a bucco-lingual dimension of less than 2 mm at the alveolar crest level, which is considered as the knife-edge ridge according to Pietrokovski et al.[21].

The image was plotted and used to determine x and y coordinates for points that describe the outline of the external cortical bone surface. These coordinates were imported into the FEM software (ANSYS 9.0, ANSYS Inc., PA, USA) as keypoints that were connected by smooth lines/curves using a 'spline algorithm'. The area was divided into a cancellous core surrounded by a layer of cortical bone. Two basic bone models (Knife models) were created with exactly the same external cortical bone outline, but different cortical bone thicknesses at the crestal region. The first had a uniform layer of cortical bone 1.6 mm thick (thin group), and the second had cortical bone thickness at the crestal region of 3.2 mm (thick group). The two-dimensional images were extruded in the z axis to create a 3D bone model with a mesio-distal length of 20 mm. The alveolar bone models were approximately 12.25 mm wide bucco-lingually and 28.5 mm heigh infero-superiorly.

Flattening and several levels of osteoplasty were simulated for the two basic Knife alveolar bone models by gradually subtracting the bone in the crestal region until a flattened surface was obtained in the Flat models, with 1 mm of bone on the buccal and distal sides. A vertical distance of 0.5 mm (measured from the highest point vertically) was removed each time to produce the Reduction models: R1, R2, R3, R4 and R5 (Fig. 1). The reduction was performed in a curved way to preserve the bucco-lingual width and was limited to the central part of the bone segment with a mesio-distal length of 8 mm, corresponding to the standard implant diameter (4 mm) and 2 mm on both mesial and distal sides. 14 models were constructed (Fig. 1). A cylindrical implant, 4 mm in diameter and 10 mm long, was placed vertically in the alveolar ridge, with a simplified abutment and crown, 6 mm in diameter and 8 mm high.

Loading and boundary conditions

All materials were assumed to be isotropic, homogeneous and linearly elastic. The interfaces between the materials were assumed bonded or osseointegrated. Young's moduli of the cortical bone, cancellous bone, implant, and prosthetic structures were assumed to be 15 GPa, 1.5 GPa, 110 GPa and 96.6 GPa, respectively. A Poisson's ratio of 0.3 was used for all the materials, except for the prosthetic structures, which had a ratio of 0.35[9].

The models were fixed in all directions on the mesial and distal surfaces of the bone[23]. A load of 200 N applied 30°

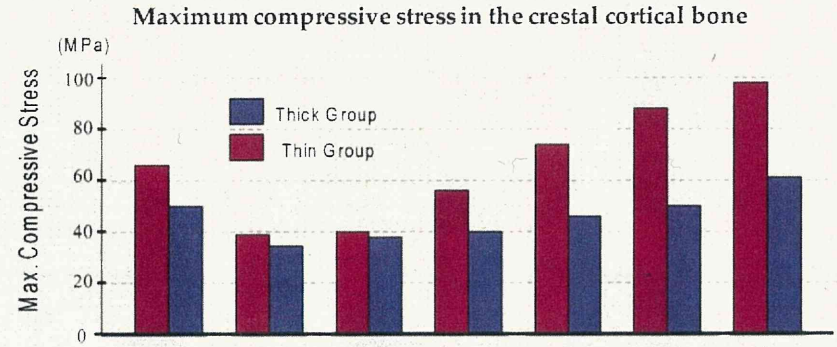

		Knife edge	R-1	R-2	R-3	R-4	R-5	Flat
Cortical Bone thickness (mm)	Thick	3.2	2.7	2.2	1.7	1.2	0.7	0.2
	Thin	1.6	1.1	0.6	0.1	0.0	0.0	0.0

Fig. 2. Maximum compressive stress values (MPa) in the crestal bone around the necks of the implants on application of the oblique loads: Thin, thin cortical bone group; thick, thick cortical bone group. The thickness of the crestal cortical bone at the midline is shown in each model of the two groups.

buccal from the vertical axis[15] was applied at the center of the occlusal surface of the crown.

All models were meshed with 20-node tetrahedral elements. A convergence test was performed to determine the number of elements to ensure the validity of calculations. A finer mesh was generated around the neck of the implant. Depending on the model, element numbers ranges were 75,175–82,793 and 90,435–98,328 in the thick and thin groups, respectively. The compressive stress and strain results were calculated and recorded for all models in the bone structures.

Results

The maximum compressive stress and strain values in each of the 14 models are summarized in Figs 2 and 3. On loading the implant, maximum compressive stresses were observed at the cervical region of the cortical bone in all models. In the knife-edge models, the maximum stress was noted at the mesial and distal sides of the implant neck on the sharp bone edge (Figs 4 and 5). Maximum cortical bone stress values were 49.5 MPa and 66.3 MPa in the thick and thin models, respectively. A marked reduction in stress was noted when the sharp edge was eliminated in R1 models with peak compressive stress of 36.8 MPa and 38.9 MPa for thick and thin cortical bone models, respectively. The maximum compressive stress was increased progressively as the alveolar crest height became reduced. The highest compressive stress value occurred around the implant in the flat models with 60.8 MPa and 98.3 MPa in the thick and thin cortical bone models, respectively (Figs 4 and 5).

In the cancellous bone, the maximum stress values were considerably lower than those in the cortical bone in all models. Peak stresses were observed at the crestal region under the cortical bone plate around the implant neck in R3, R4, R5 and Flat models of the thin group and the Flat model of the thick group. In the rest of the models, peak stresses were observed at the lingual side of the implant apex (Fig. 6). The distribution of the maximum compressive strain was similar to the compressive stress in the corresponding models.

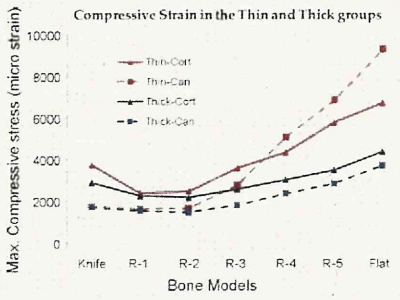

Fig. 3. The maximum compressive strain values (micro strain) in the cortical and cancellous bones in each model of the thin and thick groups. Cort-Thin, cortical bone in the thin group; Canc-Thin, cancellous bone in the thin group; Cort-Thick, cortical bone in the thick group; Canc-thick, cancellous bone in the thick group.

Discussion

FEA is used increasingly to predict the performance of dental implants. It can be undertaken by studying mechanical parameters such as the stress or strain generated in the implant and surrounding bone structures[9]. FEA comprises several steps starting with the pre-processing stage, in which the implant and bone models are developed. To obtain accurate results and precisely evaluate the biomechanical aspects of treatment options, it is essential to develop and design models that represent clinical conditions. Previous FEA studies have tended to ignore the local anatomy of the crestal bone and implant site preparation, for example by representing the alveolar bone with a simplified rectangle in two dimensions or a block with rectangular cross-section in 3D models. When anatomical models are used, the crestal region is often modified to have a flat contour with a uniform cortical bone layer. Recently, more accurate, realistic models have been constructed using CT scan data and other advanced digital imaging techniques. The data used are commonly selected for the ideal bone morphology of a well rounded alveolar bone (class III Cawood and Howell classification[4]) which does not represent other bone morphology types.

Pietrokoviski et al.[21] investigated the characteristics of edentulous ridges in

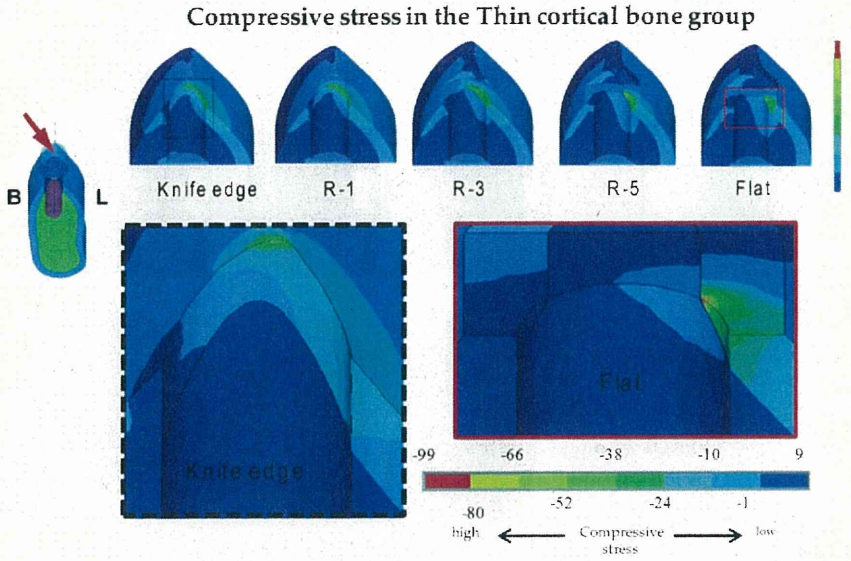

Fig. 4. The effects of gradual reduction of the alveolar bone crest and the exposure of cancellous bone on the compressive stress in the thin cortical bone group. The figure on the left indicates the viewing angle and force direction (red arrow). Models are sectioned halves and viewed from the mesial side (upper graphics). The crestal regions in the Knife-edge and Flat models are enlarged (lower graphics). The same contour scale was used for all models in the thin group. The red area represents the highest compressive stress.

human jaws. They reported 43% with a knife-edge alveolar crest in the mandible and 38% in the premolar region. Osteoplasty procedures in which the alveolar crest is surgically reduced or flattened are considered to be the most common approach that routinely restores the required width for implant placement in thin and/or knife-edge ridges[17]. In this study, bone models represented class IV (knife-edge ridge) and different levels of osteoplasty.

Altering the morphology and geometry of the crestal bone by osteoplasty procedures was found to influence the distribution and magnitude of generated peri-implant bone stress and strain. In the knife-edge models, a relatively high compressive stress was found at the mesial and distal sides of the implant neck, where the sharp, thin edge is located. Lower stress, with an even distribution, was observed at the lingual side. The strong, bony curvature (characterized by the acute angle, measured between the vertical axis of the implant and the external lingual cervical bone surfaces) presented at the lingual side probably accounts for the reduction of stress at this region; when implants are attached to a cortical bone with stronger curvature, stress will be directed from the outer cortical edge to the inner bone[11,24]. As the sharp edge was eliminated in R1 models, the stress generated was redistributed over a larger area. Thus the maximum stress was reduced in

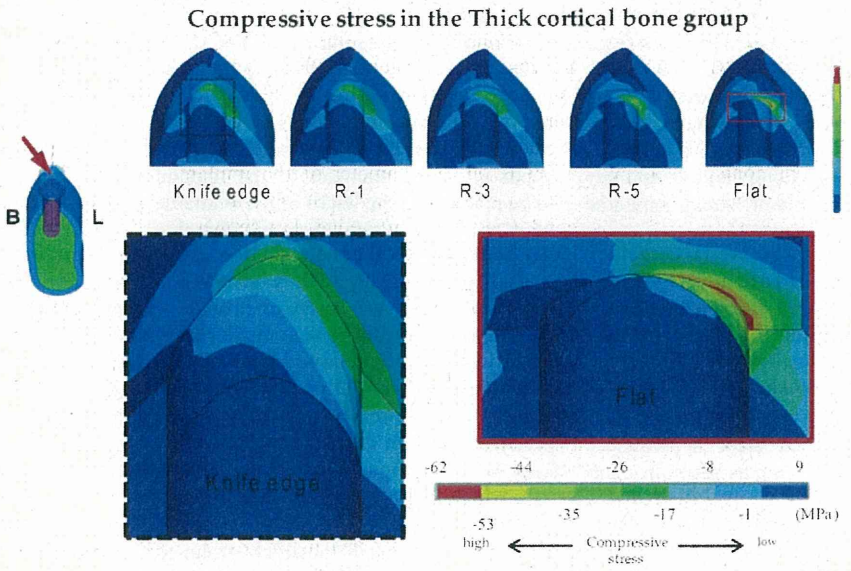

Fig. 5. The effects of gradual reduction of the alveolar bone crest on the compressive stress in the thick cortical bone group. The crestal regions in the Knife-edge and Flat models are enlarged (lower graphics). The same contour scale was used for all models in the thick group.

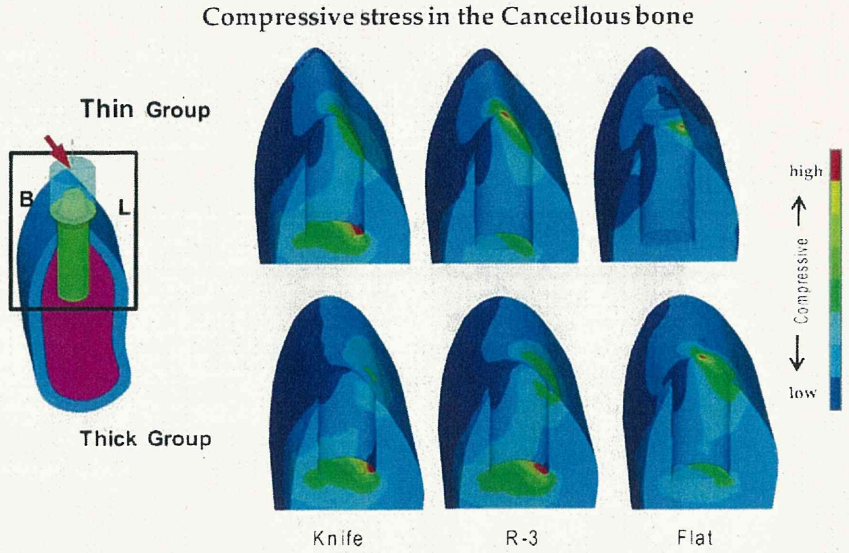

Fig. 6. The compressive stress distributions in the cancellous bone were shown in the Knife edge, R3, and Flat models of the thick (upper graphics) and thin (lower graphics) groups sectioned halves and viewed from the mesial side. Red contour represents the maximum stress in each model. (For interpretation of the references to color in this figure legend, the reader is referred to the web version of the article.)

the mesial and distal regions around the implant. Maintaining the strong curvature lingually in these models (R1) may explain the preservation of the low stress level, which was evenly distributed on the lingual side. A progressive increase of stress was observed in the rest of the models as the curvature strength and the cortical bone thickness were reduced further.

Reduction of crestal bone curvature increased the resultant stress and strain, regardless of the cortical bone thickness. This was confirmed when comparing different bone reduction levels. For instance, the thick R4 model showed a higher maximum stress value than the thin R2 model, although the cortical bone thickness in the former was two times larger than the latter (Fig. 2). This demonstrates the importance of the crestal bone contour as a key factor in the resultant stress outcome around dental implants.

Bone models with larger crestal cortical bone thickness exhibited a relatively lower peri-implant stress and strain compared with the corresponding models with the same osteoplasty reduction levels but with less cortical bone thickness. This agrees with previous reports in the literature[10,20].

When the alveolar crest is surgically reduced or flattened, it may result in sharp edges to the remaining cortical bone and exposure of the cancellous bone. These changes in the bone could lead to local stress and strain concentrations and fatigue failures[8]. This would explain why the maximum stress was located at the sharp cortical edges along with the substantial increase in stress and strain values in the R3, R4, R5 and Flat models in the thin cortical bone group.

The distribution of peak stresses in the cancellous bone was influenced by the presence and the thickness of the cortical bone layer. In bone models with compromised cortical bone thickness (thin R3, and thick Flat) or with uncovered cancellous bone (thin R4, R5 and Flat), maximum stresses were found at the crestal region. This might be due to the inward displacement of the thin cortical bone plate in those models.

Osteoplasty procedures resulted in reduction of the cortical bone support/thickness and/or exposure of the cancellous bone to direct forces in the crestal region. The amount of bone reduction depends on the diameter of the implant to be placed and the width of the available bone. Class IV (knife-edge) has shown a larger need for crestal bone reduction[7]. In this study, an implant with a standard diameter of 4 mm was used to provide the 1 mm of supporting bone at the buccal and lingual sides, the required bucco-lingual width was 6 mm. Depending on the thickness of the cortical bone layer, osteoplasty may result in exposing the cancellous bone as demonstrated in the thin group, which represents the average cortical bone thickness. The crestal cortical bone was doubled in the thick group to study the influence of gradual reduction and flattening with and without cancellous bone exposure.

The potential fatigue damage to the bone is expected to occur under excessive dynamic loading that exceeds 4000 microstrain under compressive forces[8,18]. This is attributed to the accumulation of induced micro-damage that exceeds the bone repair capacity[2,8]. The compressive stress and strain parameters were used as a risk scale in this study but inherent simplifications made in FEA may limit the direct application of quantitative results obtained from these analyses.

The aim of this study was not to predict the exact *in vivo* stresses, but to explore the possible differences that result as a consequence of modifying crestal bone morphology. Limitations of this study include single static loading and the vertical placement of the implant and the bone quality used. Previous studies have indicated that in comparative analysis, the relative accuracy of the results is not affected by these parameters[14]. A cylindrical non-threaded implant was used in this study as it is considered the neutral design[1], and to establish a baseline from which other implant designs can be compared in further studies. The implant–bone attachment was assumed to be perfectly and continuously bonded. This is because of the absence of reliable data regarding the interfacial tensile strength.

In this study, the stress and strain generated around the dental implant were investigated immediately after osseointegration. Accordingly, neither bone resorption nor corticalization was represented. The central region of cancellous bone was

uncovered in some models, but the cortical bone support that is considered critical for implant stability was maintained for implants in all models.

Based on the results of this study, osteoplasty procedures may critically affect the stress and strain outcomes in the peri-implant bone structure. The high stress and strain generated around dental implants could cause mechanical overloading of the bone and may result in alveolar bone loss that affects the long term success of the implant treatment. Exposing the cancellous bone has significantly increased cancellous bone strain around the implant. Accordingly, from a biomechanical point of view, a sharp edge should be carefully eliminated while flattening the crestal region and uncovering cancellous bone should be avoided.

Rounding or reduction of the alveolar bone may redistribute and decrease the stress. Based on the results of this study, and taking into consideration the wide variation in bone morphology and cortical bone thickness among individuals, it may be impossible to draw a definitive conclusion regarding the limit to which the crestal region can be reduced without causing considerable increase in the resultant stresses.

When the alveolar bone ridge is rounded or flattened, the available bone height for implant placement is reduced. Consequently, shorter implants are placed in these ridges[7,17]. Simultaneously, the crown height space is increased. This change in the crown/implant ratio increases the stress generated in the peri-implant bone structures[22]. In the current study, the intrabony implant length and the supra-crestal abutment and prosthesis heights were standardized to exclude the effect of crown/implant ratio.

In conclusion, crestal bone osteoplasty procedures performed prior to implant placement may improve the resultant stress and strain outcomes around the dental implant neck when the sharp edge of the knife-edge ridge is eliminated. Flattening the alveolar crest and uncovering the cancellous bone may have the disadvantage of significantly increasing stress and strain in the crestal bone region.

Funding

None.

Competing interests

None declared.

Ethical approval

Not required.

Acknowledgements. The authors would like to thank Dr. N. Wakabayashi and Prof. T. J. Wright for their helpful comments.

References

1. Abu-Hammad O, Khraisat A, Dar-Odeh N, El-Maaytah M. Effect of dental implant cross-sectional design on cortical bone structure using finite element analysis. Clin Implant Dent Relat Res 2007: **9**: 217–221 doi CID048 [pii] 10.1111/j.1708-8208.2007.00048.x.
2. Brunski JB. In vivo bone response to biomechanical loading at the bone/dental–implant interface. Adv Dent Res 1999: **13**: 99–119.
3. Buser D, Bragger U, Lang NP, Nyman S. Regeneration and enlargement of jaw bone using guided tissue regeneration. Clin Oral Implants Res 1990: **1**: 22–32.
4. Cawood JI, Howell RA. A classification of the edentulous jaws. Int J Oral Maxillofac Surg 1988: **17**: 232–236.
5. Chiapasco M, Romeo E, Vogel G. Tridimensional reconstruction of knife-edge edentulous maxillae by sinus elevation, onlay grafts, and sagittal osteotomy of the anterior maxilla: preliminary surgical and prosthetic results. Int J Oral Maxillofac Implants 1998: **13**: 394–399.
6. Duyck J, Ronold HJ, Van Oosterwyck H, Naert I, Vander Sloten J, Ellingsen JE. The influence of static and dynamic loading on marginal bone reactions around osseointegrated implants: an animal experimental study. Clin Oral Implants Res 2001: **12**: 207–218 doi clr120304 [pii].
7. Eufinger H, Konig S, Eufinger A. The role of alveolar ridge width in dental implantology. Clin Oral Investig 1997: **1**: 169–177.
8. Frost HM. A brief review for orthopedic surgeons: fatigue damage (microdamage) in bone (its determinants and clinical implications). J Orthop Sci 1998: **3**: 272–281.
9. Geng JP, Tan KB, Liu GR. Application of finite element analysis in implant dentistry: a review of the literature. J Prosthet Dent 2001: **85**: 585–598 doi S0022-3913(01)57431-4 [pii] 10.1067/mpr.2001.115251.
10. Holmes DC, Loftus JT. Influence of bone quality on stress distribution for endosseous implants. J Oral Implantol 1997: **23**: 104–111.
11. Hylander WL. Mandibular function and biomechanichal stress and scaling. Am Zool 1985: **25**: 223–240.
12. Kim Y, Oh TJ, Misch CE, Wang HL. Occlusal considerations in implant therapy: clinical guidelines with biomechanical rationale. Clin Oral Implants Res 2005: **16**: 26–35 doi CLR1067 [pii]10.1111/j.1600-0501.2004.01067.x.
13. Lekholm U, Adell R, Lindhe J, Branemark PI, Eriksson B, Rockler B, Lindvall AM, Yoneyama T. Marginal tissue reactions at osseointegrated titanium fixtures. II. A cross-sectional retrospective study. Int J Oral Maxillofac Surg 1986: **15**: 53–61.
14. Meijer HJ, Starmans FJ, Steen WH, Bosman F. A three-dimensional, finite-element analysis of bone around dental implants in an edentulous human mandible. Arch Oral Biol 1993: **38**: 491–496 doi 0003-9969(93)90185-O [pii].
15. Mericske-Stern R, Assal P, Mericske E, Burgin W. Occlusal force and oral tactile sensibility measured in partially edentulous patients with ITI implants. Int J Oral Maxillofac Implants 1995: **10**: 345–353.
16. Misch CE. Available bone and dental implant treatment plans. In: Misch CE, ed: Contemporary Implant Dentistry. St. Louis: Mosby Elsevier 2008 : 178–194.
17. Misch CE. Divisions of available bone in implant dentistry. Int J Oral Implantol 1990: **7**: 9–17.
18. Mosley JR, Lanyon LE. Strain rate as a controlling influence on adaptive modeling in response to dynamic loading of the ulna in growing male rats. Bone 1998: **23**: 313–318 doi S8756-3282(98)00113-6 [pii].
19. Nagasao T, Kobayashi M, Tsuchiya Y, Kaneko T, Nakajima T. Finite element analysis of the stresses around fixtures in various reconstructed mandibular models – part II (effect of horizontal load). J Craniomaxillofac Surg 2003: **31**: 168–175 doi S1010518203000295 [pii].
20. Petrie CS, Williams JL. Probabilistic analysis of peri-implant strain predictions as influenced by uncertainties in bone properties and occlusal forces. Clin Oral Implants Res 2007: **18**: 611–619 doi CLR1384 [pii] 10.1111/j.1600-0501.2007.01384.x.
21. Pietrokovski J, Starinsky R, Arensburg B, Kaffe I. Morphologic characteristics of bony edentulous jaws. J Prosthodont 2007: **16**: 141–147 doi JOPR165 [pii] 10.1111/j.1532-849X.2007.00165.x.
22. Tada S, Stegaroiu R, Kitamura E, Miyakawa O, Kusakari H. Influence of implant design and bone quality on stress/strain distribution in bone around implants: a 3-dimensional finite element analysis. Int J Oral Maxillofac Implants 2003: **18**: 357–368.
23. Teixeira ER, Sato Y, Akagawa Y, Shindoi N. A comparative evaluation of mandibular finite element models with different lengths and elements for implant biomechanics. J Oral Rehabil 1998: **25**: 299–303.
24. van Eijden TM. Biomechanics of the mandible. Crit Rev Oral Biol Med 2000: **11**: 123–136.
25. Watzak G, Zechner W, Tepper G, Vasak C, Busenlechner D, Bernhart

T. Clinical study of horizontal alveolar distraction with modified micro bone screws and subsequent implant placement. Clin Oral Implants Res 2006: **17**: 723–729 doi CLR1267 [pii] 10.1111/j.1600-0501.2006.01267.x.

Address:
Malik Hudieb
Department of Oral Implantology and Regenerative Dental Medicine
Division of Oral Health Sciences
Graduate School
Tokyo Medical and Dental University
1-5-45 Yushima
Bunkyo
Tokyo 113-8549
Japan
Tel.: +81 358034664
fax: +81 358034664.
E-mail: mhudeab@gmail.com

Fully functional bioengineered tooth replacement as an organ replacement therapy

Etsuko Ikeda[a,b,1], Ritsuko Morita[a,c,1], Kazuhisa Nakao[a,c], Kentaro Ishida[a,c], Takashi Nakamura[a,c], Teruko Takano-Yamamoto[d], Miho Ogawa[b], Mitsumasa Mizuno[a,c,d], Shohei Kasugai[e], and Takashi Tsuji[a,b,c,2]

[a]Department of Biological Science and Technology, Faculty of Industrial Science and Technology, and [c]Research Institute for Science and Technology, Tokyo University of Science, Noda, Chiba 278-8510, Japan; [b]Organ Technologies Inc., Tokyo 101-0048, Japan; [d]Division of Orthodontics and Dentofacial Orthopedics, Graduate School of Dentistry, Tohoku University, Sendai, Miyagi 980-8575, Japan; and [e]Oral and Maxillofacial Surgery, Department of Oral Restitution, Division of Oral Health Sciences, Graduate School, Tokyo Medical and Dental University, Tokyo 113-8510, Japan

Edited by Robert Langer, Massachusetts Institute of Technology, Cambridge, MA, and approved June 30, 2009 (received for review March 17, 2009)

Current approaches to the development of regenerative therapies have been influenced by our understanding of embryonic development, stem cell biology, and tissue engineering technology. The ultimate goal of regenerative therapy is to develop fully functioning bioengineered organs which work in cooperation with surrounding tissues to replace organs that were lost or damaged as a result of disease, injury, or aging. Here, we report a successful fully functioning tooth replacement in an adult mouse achieved through the transplantation of bioengineered tooth germ into the alveolar bone in the lost tooth region. We propose this technology as a model for future organ replacement therapies. The bioengineered tooth, which was erupted and occluded, had the correct tooth structure, hardness of mineralized tissues for mastication, and response to noxious stimulations such as mechanical stress and pain in cooperation with other oral and maxillofacial tissues. This study represents a substantial advance and emphasizes the potential for bioengineered organ replacement in future regenerative therapies.

regenerative therapy | transplantation

The current approaches being used to develop future regenerative therapies are influenced by our understanding of embryonic development, stem cell biology, and tissue engineering technology (1–4). One of the more attractive concepts under consideration in regenerative therapy is stem cell transplantation of enriched or purified tissue-derived stem cells (5), or in vitro manipulated embryonic stem (ES) and induced pluripotent stem (iPS) cells (6, 7). This therapy has the potential to restore the partial loss of organ function by replacing hematopoietic stem cells in hematopoietic malignancies (8), neural stem cells in Parkinson's disease (9), mesenchymal stem cells in myocardial infarction (10), and hepatic stem cells in cases of hepatic insufficiency (11).

The ultimate goal of regenerative therapy is to develop fully functioning bioengineered organs that can replace lost or damaged organs following disease, injury, or aging (4, 12–14). The feasibility of this concept has essentially been demonstrated by successful organ transplantations for various injuries and diseases (15). It is expected that bioengineering technology will be developed for the reconstruction of fully functional organs in vitro through the precise arrangement of several different cell species. However, these technologies have not yet achieved 3-dimensional reconstructions of fully functioning organs. To achieve the functional replacement of lost or damaged tissues and organs, the development of 3-dimensional bioengineered tissues comprising a single cell type is now being attempted using biodegradative materials (3), appropriate cell aggregation (16), or uniform cell sheets (17). These are now clinically applied for corneal dysfunction (18), myocardial infarction (19), and hepatic insufficiency (20) using oral mucosal epithelial cells, myocardial cells, and liver cells, respectively, with favorable clinical results.

A concept has also now been proposed to develop a bioengineered organ by reproducing the developmental processes during organogenesis (13, 21, 22). Almost all organs arise from their respective germs through reciprocal interactions between the epithelium and mesenchyme in the developing embryo (23–25). Therefore, it is predicted that a functional bioengineered organ could be produced by reconstituting organ germs between epithelial and mesenchymal cells in vitro, although the existence of organ-inductive stem cells in the adult body has not been fully elucidated yet with the exception of hair follicles (26) and the mammary gland (27). Tooth replacement regenerative therapy, which is also induced by typical reciprocal epithelial, and mesenchymal interactions (25, 28), is thought to be a feasible model system to evaluate the future clinical application of bioengineered organ replacement (13, 21). The strategy to develop a bioengineered third tooth after the loss of deciduous and permanent teeth is to properly reproduce the processes which occur during embryonic development through the reconstitution of a bioengineered tooth germ in vitro (21). We have recently developed a method for creating 3-dimensional bioengineered organ germ, which can be used as an ectodermal organ such as the tooth or whisker follicle (29). Our analyses have provided an effective method for reconstituting this organ germ and raised the possibility of tooth replacement with integrated blood vessels and nerve fibers in an adult oral environment (29). However, it remains to be determined whether a bioengineered tooth can achieve full functionality, including sufficient masticatory performance, biomechanical cooperation with tissues in the oral and maxillofacial regions, and proper responsiveness via sensory receptors to noxious stimulations in the maxillofacial region. There are currently no published reports describing successful replacement with a fully functional bioengineered organ.

In our current study, we describe a fully functioning tooth replacement achieved by transplantation of a bioengineered tooth germ into the alveolar bone of a lost tooth region in an adult mouse. We propose this as a model for future organ replacement therapy. The bioengineered tooth, which was erupted and reached occlusion in the oral environment, had the correct tooth structure, hardness of mineralized tissues for mastication, and responsiveness to experimental orthodontic treatment and noxious stimulation in cooperation with tissues in the oral and maxillofacial regions. Our results thus demonstrate

Author contributions: T.T. designed research; E.I., R.M., and K.N. performed research; E.I., K.N., T.T.-Y., and S.K. contributed new reagents/analytic tools; E.I., R.M., K.N., K.I., T.N., M.O., and M.M. analyzed data; and E.I., R.M., K.N., and T.T. wrote the paper.

The authors declare no conflict of interest.

This article is a PNAS Direct Submission.

Freely available online through the PNAS open access option.

[1]E.I. and R.M. contributed equally to this work.

[2]To whom correspondence should be addressed. E-mail: t-tsuji@rs.noda.tus.ac.jp.

This article contains supporting information online at www.pnas.org/cgi/content/full/0902944106/DCSupplemental.

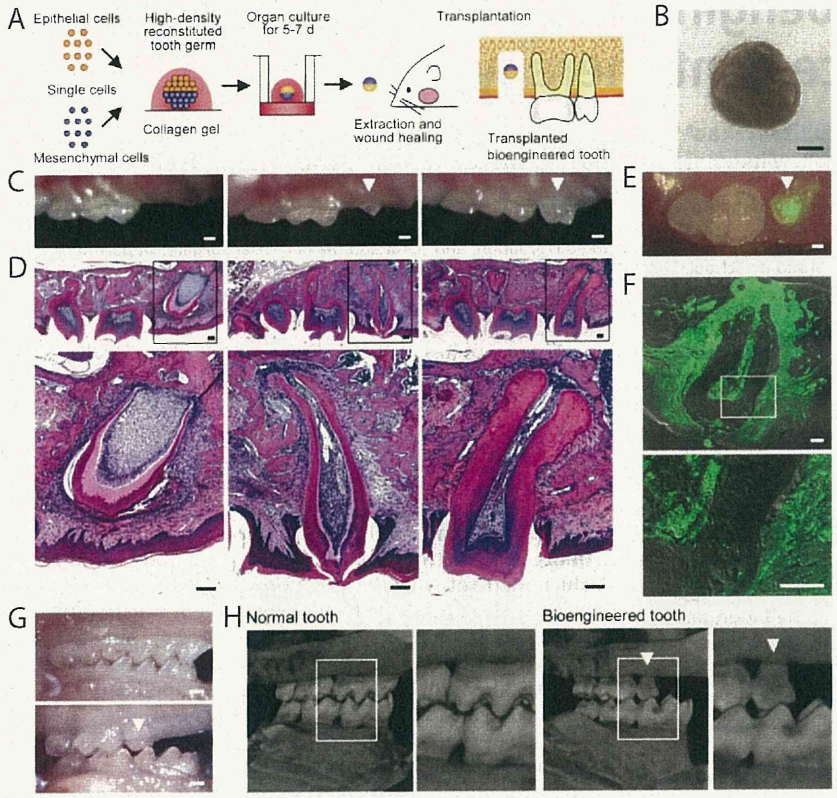

Fig. 1. Eruption and occlusion of a bioengineered tooth. (*A*) Schematic representation of the transplantation technology used for the generation of reconstituted tooth germ. (*B*) Phase contrast image of bioengineered tooth germ on day 5 of an organ culture. (Scale bar, 200 μm.) (*C*) Oral photographs of a bioengineered tooth during eruption and occlusion processes, including before eruption (*Left*), immediately after eruption (*Center*), and full occlusion (*Right*). (Scale bar, 200 μm.) (*D*) Histological analysis of the bioengineered tooth during the eruption and occlusion processes, including before eruption (*Left*), immediately after eruption (*Center*), and full occlusion (*Right*). (Scale bar, 100 μm.) (*E*) Oral photograph of a bioengineered tooth reconstituted using a combination of epithelial cells from normal mice and mesenchymal cells from GFP-transgenic mice (GFP bioengineered tooth). A merged image is shown. (Scale bar, 200 μm.) (*F*) A sectional image of a GFP bioengineered tooth. Fluorescent and DIC images are merged. (Scale bar, 100 μm.) (*G*) Oral photographs showing occlusion of normal (*Upper*) and bioengineered (*Lower*) teeth. (Scale bar, 200 μm.) (*H*) MicroCT images of the occlusion of normal (*Left*) and bioengineered (*Right*) teeth. External (*Left*) and cross section (*Right*) images are shown. The bioengineered tooth is indicated by the arrowhead.

the potential of bioengineered organ replacement for use in future regenerative therapies.

Results

Eruption and Occlusion of a Bioengineered Tooth. We first investigated whether a bioengineered molar tooth germ, which was reconstituted from embryonic day 14.5 (ED14.5) molar tooth germ-derived epithelial and mesenchymal cells by our previously developed organ germ method, could erupt and reach occlusion with an opposing tooth in the mouse adult oral environment (Fig. 1*A*). After 5–7 days in an organ culture, a single bioengineered molar tooth germ, which had developed at the early bell stage of a natural tooth germ and was with a mean length of 534.4 ± 45.6 μm (Fig. 1*B*), was then transplanted with the correct orientation into a properly-sized bony hole in the upper first molar region of the alveolar bone in an 8-week-old adult murine lost tooth transplantation model. In this model, the upper first molar had been extracted, and the resulting wounds had been allowed to heal for 3 weeks (Fig. 1*A* and Fig. S1*A*). The cusp tip of the bioengineered tooth was exposed into the oral cavity at 36.7 ± 5.5 days after transplantation at a frequency of 34/60 (56.6%) (Fig. 1*C Center* and Fig. S1 *B–D Center*). In current transplantation model, the non-erupted explants also occurred at low frequency and were due to the microsurgery for the transplantation, such as transplantation with the reverse direction or the falling off the explants. The vertical dimension of the tooth crown continually increased and the bioengineered tooth finally reached the plane of occlusion with the opposing lower first molar at 49.2 ± 5.5 days after transplantation (Fig. 1*C Right*, and Fig. S1 *B–D Right* and *E*). During the course of eruption and occlusion, the alveolar bone at the bony hole gradually healed in the areas around the bioengineered tooth and the regenerated tooth had sufficient periodontal space between itself and the alveolar bone (Fig. 1*D* and Fig. S1*D*). The bioengineered tooth also formed a correct structure comprising enamel, ameloblast, dentin, odontoblast, dental pulp, alveolar bone, and blood vessels (Fig. 1*D*). It is known that mice have a considerable amount of cellular cementum that increases in thickness both on the sides of the roots and in the interradicular area and forms around the apex of the molar roots (30). The fully occluded bioengineered tooth was also observed to have a large amount of cellular cementum that was equivalent to a normal murine molar tooth (Fig. 1*D* and Fig. S1*A*). The root of the bioengineered tooth was also observed to be surrounded by sufficient periodontal ligaments (PDL) (Fig. 1*D*). Observations of the bioengineered tooth morphology revealed that the crown had plural cusp structure. The lengths and crown widths of the erupted bioengineered teeth were 1,474.4 ± 115.1 and 690.7 ± 177.7 μm, respectively. However, the bioengineered tooth was smaller than the other normal teeth, since at present we cannot regulate the crown width, cusp position, and tooth patterning including anterior/posterior and buccal/lingual structures using in vitro cell manipulation techniques.

We also transplanted green fluorescence protein (GFP)-labeled bioengineered tooth germ, which was reconstituted by normal epithelial cells and the mesenchymal cells from GFP-transgenic mice into non-transgenic mice as described above (29). A GFP-labeled bioengineered tooth was produced and could be observed in the bony hole in the alveolar bone of adult mice (Fig. 1*E* and Fig. S1*F*). GFP-positive mesenchymal cells were also detectable both in the odontoblasts and in the dental pulp and PDL, which differentiate from the dental papilla and dental follicle cells, respectively (Fig. 1*F*). Green fluorescence was also observed in the dentinal tubules of the GFP-positive odontoblasts in the regenerated tooth (Fig. 1*F Lower*).

We next investigated the gene expression profiles of colony-stimulating factor 1 (*Csf1*) and parathyroid hormone receptor (*Pthr1*), which are thought to regulate osteoclastogenesis during

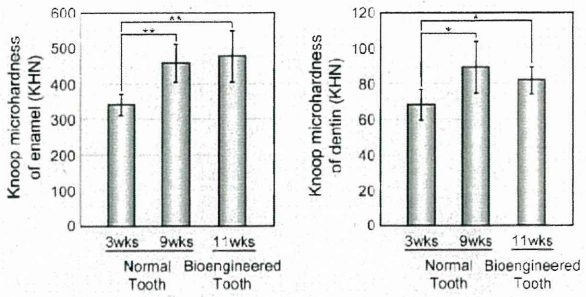

Fig. 2. Assessment of the hardness of the bioengineered tooth. Knoop microhardness values of the enamel (*Left*) and dentin (*Right*) of the bioengineered tooth at 11-weeks post transplantation were compared with those of normal teeth from 3- and 9-week-old mice. Error bars show the standard deviation ($n = 3$). $P < 0.001$ (*) and <0.0001 (**) was regarded as statistically significant (t test).

tooth eruption (31). Those genes were detectable in the eruption pathway and at the boundary surface between the dental follicle of the bioengineered tooth and osseous tissues, as is seen in normal teeth (Fig. S2). These observations suggest that the eruption of the bioengineered tooth germ faithfully reproduced the molecular mechanisms involved in the normal tooth eruption process.

We next analyzed the occlusion established between the bioengineered tooth and the opposing lower teeth. We often observed that the bioengineered tooth moved physiologically before achieving the occlusion during the transplantation experiments. The regenerated tooth achieved normal occlusion in harmony with other teeth in the recipient animal and had opposing cuspal contacts that maintained the proper occlusal vertical dimensions between the opposing arches (Fig. 1 *G* and *H*, and Fig. S1 *B–E*). Following the achievement of occlusion at 49.2 ± 5.5 days after transplantation, there was no excessive increase in the tooth length or perforation of the maxillary sinus by the erupted bioengineered tooth at up to 120 days after transplantation. These results indicated that the bioengineered tooth moved in response to mechanical stress and achieved functional occlusion with the opposing natural tooth.

Masticatory Potential of the Bioengineered Tooth. The masticatory potential of a bioengineered tooth is essential for achieving proper tooth function (32). We thus performed a Knoop hardness test, which is a test for mechanical hardness and is used in particular for very brittle materials or thin sheets. This was an important parameter for evaluating masticatory functions in our bioengineered tooth, including both the dentin and the enamel components. The Knoop hardness of both the enamel and dentin of normal teeth in 3-week-old and 9-week-old mice significantly increases in according to the postnatal period (Fig. 2). These values for enamel and dentin in the normal teeth of 9-week-old adult mice were measured at 447.7 ± 88.9 and 88.4 ± 10.2 Knoop hardness number (KHN), respectively (Fig. 2). The same measurements in the bioengineered tooth were 461.1 ± 83.2 and 81.4 ± 7.53 KHN, respectively (Fig. 2). These findings indicated that the hardness of the bioengineered tooth is in the normal range.

Bioengineered Tooth Response to Mechanical Stress. It has been postulated that regeneration of a fully functional tooth could be achieved by fulfilling critical functions in an adult oral environment such as the cooperation of the bioengineered tooth with the oral and maxillofacial regions through the PDL (31, 33). Histochemical analysis of the PDL of our bioengineered tooth (Fig. 1*D*) showed a positive connection between this tooth and the

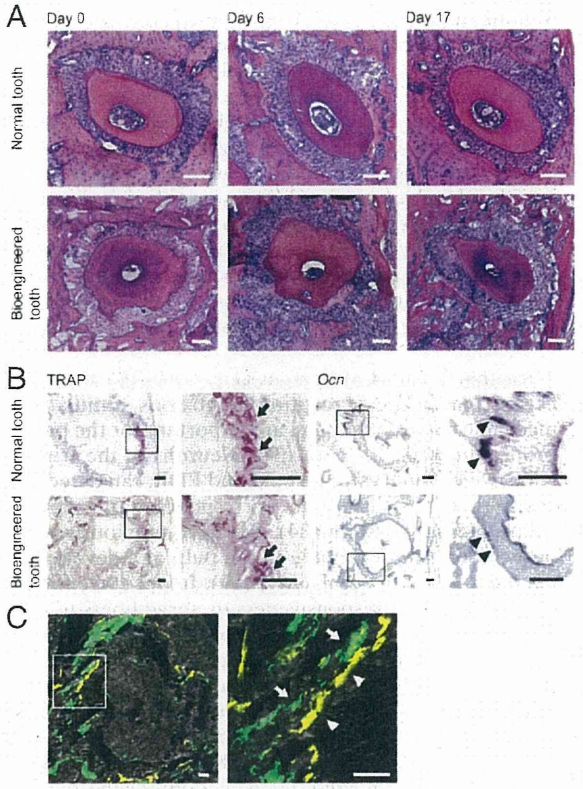

Fig. 3. Experimental tooth movement. (*A*) Horizontal sections of the root of a normal tooth (*Upper*) and a bioengineered tooth (*Lower*) were analyzed by hematoxylin-eosin staining (HE) at days 0 (*Left*), 6 (*Center*), and 17 (*Right*) of experimental orthodontic treatment. (Scale bar, 100 μm.) (*B*) Sections of a normal and bioengineered tooth were analyzed by TRAP staining and in situ hybridization of *Ocn* at day 6 of the orthodontic treatment. TRAP-positive cells (arrow) and *Ocn* mRNA-positive cells (arrowhead) are indicated. (Scale bar, 100 μm.) (*C*) The root of the bioengineered tooth was analyzed for bone formation. The image in the box in *Left* is shown at higher magnification in *Right*. Tetracycline (arrowhead) and calcein (arrow) labeling was detectable on the tension side. (Scale bar, 50 μm.)

alveolar bone, and suggesting that this tooth may be responsive to mechanical stress. It has been demonstrated previously that alveolar bone remodeling is induced via the response of the PDL to mechanical stress such as the treatment of orthodontic movements (31, 33). These same studies have further demonstrated that the localization of osteoclasts for bone resorption and osteoblasts for bone formation can be observed in the area of compression and on the tension side, respectively (31, 33). Thus, we analyzed the movement of our bioengineered tooth and also the osteoclast and osteoblast localization for remodeling in the alveolar bone by inducing orthodontic movements experimentally.

When the bioengineered tooth was moved buccally for 17 days with a mechanical force in an experimental tooth movement model, it performed as well as a normal tooth (Fig. 3*A* and Fig. S3). Histochemical analysis additionally revealed morphological changes in the PDL in both the sides containing lingual tension and buccal compression following 6 days of treatment (Fig. 3*A* and Fig. S3). Osteoblast-like cells, which have a cuboidal shape and rounded nuclei, and osteoclast-like cells, which are multinucleated giant cells, were observed on the surface of the alveolar bone within the tension and compression sides, respectively (Fig. 3*A* and Fig. S3). During experimental tooth movement, tartrate-resistant acid phosphatase (TRAP)-positive

staining was observed in the multinucleated cells, indicating that osteoclast-like giant cells were dominant on the compression side (Fig. 3*B*). In contrast, the localization of osteocalcin (*Ocn*) mRNA-positive cells was observed in the cells on the tension side, indicating that osteoblast-like cells were dominant (Fig. 3*B*). A fluorescent double-labeling experiment using calcein and tetracycline further showed that incorporation of these reagents into the alveolar bone on the tension side, but not the compression side, was clearly observable in the double-labeled line within 10 days of the orthodontic treatment (Fig. 3*C*). These findings suggest that the PDL of the bioengineered tooth successfully mediates bone remodeling via the proper localization of osteoclasts and osteoblasts in response to mechanical stress.

Perceptive Potential of Neurons Entering the Tissue of the Bioengineered Tooth. The perception of noxious stimulations such as mechanical stress and pain, are important for the protection and proper functions of teeth (34). Neurons in the trigeminal ganglion, which innervate the pulp and PDL, can detect these stress events and transduce the corresponding perceptions to the central nervous system (34). We have previously reported that nerve fibers are detectable in the pulp of a developing bioengineered tooth in the oral cavity (29). In our current experiments, we evaluated the responsiveness of nerve fibers in the pulp and PDL of the bioengineered tooth to induced noxious stimulations.

Anti-neurofilament (NF)-immunoreactive nerve fibers were detected in the pulp, dentinal tubules, and PDL of the bioengineered tooth as in a normal tooth (Fig. 4*A* and Fig. S4). Neuropeptide Y (NPY), which is synthesized in sympathetic nerves (34), was also detected in the pulp and PDL neurons (Fig. 4*A* and Fig. S4 *C* and *D*). Calcitonin gene-related peptide (CGRP), which is synthesized in sensory nerves and is involved in sensing tooth pain (34) was also observed in both pulp and PDL neurons (Fig. 4*A* and Fig. S4 *E* and *F*). NPY and CGRP were detected in both the anti-NF positive and negative-immunoreactive neurons (Fig. 4*A* and Fig. S4 *C*–*F*).

We next evaluated the perceptive potential of these neurons in the bioengineered tooth against noxious stimulations such as orthodontic treatment and pulp stimulation. The expression of galanin, which is a neuropeptide involved in pain transmission (35), increased in response to persistent painful stimulation of the nerve terminals within the PDL of the bioengineered tooth to the same extent as in a normal tooth (Fig. 4*B*). Thus PDL nerve fibers in the bioengineered tooth appear to respond to nociceptive stimulation caused by our experimental tooth movements. Previous studies have reported that neurons expressing the proto-oncogene c-Fos protein are detectable in the superficial layers of the medullary dorsal horn following noxious stimulations such as electrical, mechanical and chemical stimulation of intraoral receptive fields involving the tooth pulp, PDL, and peripheral nerves innervating the intraoral structures (34, 35). We found in our current analyses that the c-Fos-immunoreactive neurons present in both the normal tooth and the bioengineered tooth drastically increased at 2 h after experimental tooth movement, and then gradually decreased within 48 h (Fig. 4*C*). Following pulp stimulation, positive neurons in both normal and bioengineered teeth also increased at 2 h after stimulation, but could not be detected at 48 h (Fig. 4*D*). These data indicate that the nerve fibers innervating both the pulp and PDL of the bioengineered tooth have perceptive potential for nociceptive stimulations and can transduce these events to the central nervous system (the medullary dorsal horn).

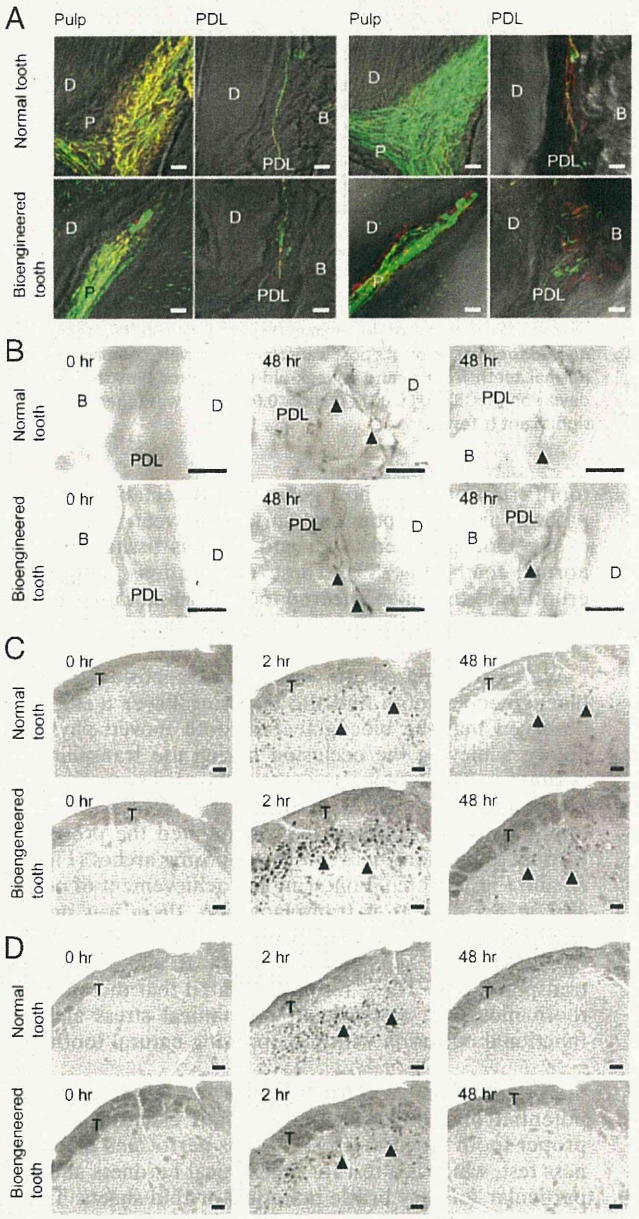

Fig. 4. Pain response to mechanical stress. (*A*) Nerve fibers in the pulp and PDL in the normal (*Upper*) and bioengineered (*Lower*) tooth were analyzed immunohistochemically using specific antibodies for the combination (left 2 columns) of NF (green) and NPY (red) and the combination (right 2 columns) of NF and CGRP (red). (Scale bar, 25 μm.) (*B*) Analysis of galanin immunoreactivity in the PDL of a normal (*Upper*) and bioengineered (*Lower*) tooth for the assessment of orthodontic force. No galanin expression was evident in the untreated tooth (*Left*). Galanin expression (arrowhead) was detected in the PDL of a normal and bioengineered tooth after 48 h of orthodontic treatment (*Right*). (Scale bar, 25 μm.) (*C*) Analysis of c-Fos-immunoreactivity in the medullary dorsal horn of mice with a normal tooth (*Upper*) or a bioengineered tooth (*Lower*) after 0 h (*Left*), 2 h (*Center*), and 48 h (*Right*) of orthodontic treatment. c-Fos expression (arrowhead) was also detected. (Scale bar, 50 μm.) (*D*) Analysis of c-Fos immunoreactivity in the medullary dorsal horn of mice with a normal tooth (*Upper*) or a bioengineered tooth (*Lower*) after 0 h (*Left*), 2 h (*Center*), and 48 h (*Right*) of stimulation by pulp exposure. c-Fos expression (arrowhead) was evident in the medullary dorsal horn after 2 and 48 h of pulp exposure. (Scale bar, 50 μm.) D, dentin; P, pulp; B, bone; PDL, periodontal ligament; T, spinal trigeminal tract.

Discussion

We successfully demonstrate herein that our bioengineered tooth germ develops into a fully functioning tooth with sufficient hardness for mastication and a functional responsiveness to mechanical stress in the maxillofacial region. We also show that the neural fibers that have re-entered the pulp and PDL tissues of the bioengineered tooth have proper perceptive potential in response to noxious stimulations such as orthodontic treatment and pulp stimulation.